Macroscopic yield in cavitated polymer blends

Pijnenburg, K.G.W.; van der Giessen, E.

Published in:
International Journal of Solids and Structures

DOI:
10.1016/S0020-7683(00)00227-4

Publication date:
2001

PERGAMON

International Journal of Solids and Structures 38 (2001) 3575–3598

INTERNATIONAL JOURNAL OF SOLIDS and STRUCTURES

www.elsevier.com/locate/ijsolstr

Macroscopic yield in cavitated polymer blends

K.G.W. Pijnenburg, E. Van der Giessen *

Laboratory of Engineering Mechanics, Koiter Institute, Delft University of Technology, Mekelweg 2, 2628 CD Delft, Netherlands

Received 19 July 1999; in revised form 14 March 2000

Abstract

Polymer blends in which the rubber particles have cavitated may be regarded as porous materials. The yield behaviour of many porous media can be well described with the Gurson model. Polymers, however, are characterized by large elastic strains prior to yield. These effects are neglected in the original Gurson formulation, which, as will be shown, leads to an overestimation of the yield stress for the voided blend. The localization of polymer plasticity in narrow shear bands also results in deviations from the standard theory. This paper presents two-dimensional cell calculations of a voided polymer and demonstrates that the overall yield characteristics are not represented well by the Gurson potential. A modification of this potential is proposed that accounts for elasticity effects and shear banding and gives better agreement with the cell results. The new potential is generalized to a full three-dimensional continuum model for voided polymer blends.

Keywords: Polymer blends; Gurson model; Gurson formulation

1. Introduction

The toughness of glassy polymers is known to be greatly enhanced by mixing in of small (1 μm or smaller) rubber particles up to volume fractions of 40%. This toughening is believed to take place due to massive plastic deformations in the polymer matrix, which become possible once the rubber particles have cavitated, thereby leaving an essentially porous material. Rather than brittle fracture by crazing, the material fails in a more ductile manner with a substantial part of the energy being dissipated by plastic flow of the matrix (e.g. Bucknall, 1977).

In order to quantify these effects, with a view to optimizing the toughening, much research has been devoted to the various steps involved. The most intensively studied step is the plastic flow around the voids left behind after cavitation of the rubber particles (Haward and Owen, 1973; Sue and Yee, 1988). Such work has gained momentum since Boyce et al. (1988) initiated realistic constitutive models for large strain plastic flow in amorphous polymers. These models account for rate and temperature dependent flow, intrinsic strain softening upon yield, followed by progressive hardening. Such models have been used for

* Corresponding author. Tel.: +31-15-278-6500; fax: +31-15-278-2150.
E-mail address: e.vanderGiessen@wbmt.tudelft.nl (E. Van der Giessen).

0020-7683/01/$ - see front matter
PII: S0020-7683(00)00227-4

instance to study the local deformations around pre-cavitated (Steenbrink et al., 1997, 1998; Smit et al., 1999; Socrate and Boyce, 2000) or uncavitated rubber particles (Steenbrink and Van der Giessen, 1999).

In analogy with the developments in ductile fracture of metals, a necessary next step would be to develop constitutive models for the overall macroscopic behaviour of cavitated, voided amorphous polymers. A necessary ingredient of this is a description of the stress-state dependence of macroscopic yield. A first attempt towards this is due to Steenbrink et al. (1997) who proposed a potential that was adopted from Gurson's (1977) yield function (also see Lazzeri and Bucknall, 1995), but adapted to the rate and temperature dependent flow of polymers.

Recent unit cell computations of a voided polymer subject to macroscopic shearing, however, revealed that the intrinsic softening of the matrix polymer gives rise to a type of localized plastic flow that is not consistent with that presumed in the Gurson model. Moreover, this deformation mode suggests a different dependence on the porosity level than according to the Gurson-type model (Steenbrink et al., 1997). The objective of this paper is to explore this in more detail, by performing unit cell computations under different stress states including shear. Following the presentation of the two-dimensional (2-D) cell model including periodic boundary conditions, we demonstrate how the plastic deformations evolve by propagating shear bands with continued macroscopic loading up to macroscopic yield and beyond. Interpretation of these deformation patterns suggests a modification of the Gurson-type potential. A second modification is necessary to account for the fact that the yield strain of polymers is relatively large (typically 5–10%). We conclude with a generalization of the macroscopic yield potential to three dimensions.

2. Material model

We model the polymer blend as a 2-D material in which the rubber particles already have cavitated. Furthermore, we assume that the rubber elastic modulus of the cavitated rubber is so low (Steenbrink and Van der Giessen, 1999) that the rubber particles can be represented as voids in the matrix material. Thus, we will be considering a porous polymer with a void volume fraction f equal to that of the volumetric rubber content of the blend. If in addition we assume the voids to be distributed in a regular square array, we can restrict our attention to a unit cell as shown in Fig. 1. The relevant morphological parameters are the particle radius, a, and half of the particle spacing, b. The ratio of a and b is related to the particle volume fraction as $f = (\pi/4)(a/b)^2$.

2.1. Method of analysis

The material is taken to be deformed macroscopically by a combination of normal strain rates $\dot{E}_{11}$ and $\dot{E}_{22}$ in the $\mathbf{e}_1$ and $\mathbf{e}_2$ direction, respectively, and by simple shear at a rate of $2\dot{E}_{12}$ parallel to the $\mathbf{e}_1$ axis. Thus, the components of the macroscopic velocity gradient L_{ij} on the basis $\{\mathbf{e}_i\}$ (corresponding to Cartesian coordinates with the origin in the centre of the void, see Fig. 1) read

$$L_{ij} = \begin{pmatrix} \dot{E}_{11} & 2\dot{E}_{12} \\ 0 & \dot{E}_{22} \end{pmatrix} \tag{1}$$

so that the macroscopic strain-rate (D_{ij}) and spin (W_{ij}) components are

$$D_{ij} = \begin{pmatrix} \dot{E}_{11} & \dot{E}_{12} \\ \dot{E}_{12} & \dot{E}_{22} \end{pmatrix}, \qquad W_{ij} = \begin{pmatrix} 0 & \dot{E}_{12} \\ -\dot{E}_{12} & 0 \end{pmatrix}. \tag{2}$$

This combination of elementary deformation modes allows to cover all possible principal directions of D_{ij} by varying the ratio between $\dot{E}_{11} - \dot{E}_{22}$ and $\dot{E}_{12}$. In general, these principal directions will not align with the principal directions $\mathbf{e}_1$ and $\mathbf{e}_2$ of the void array (except when $\dot{E}_{12} = 0$). As a consequence, the cell

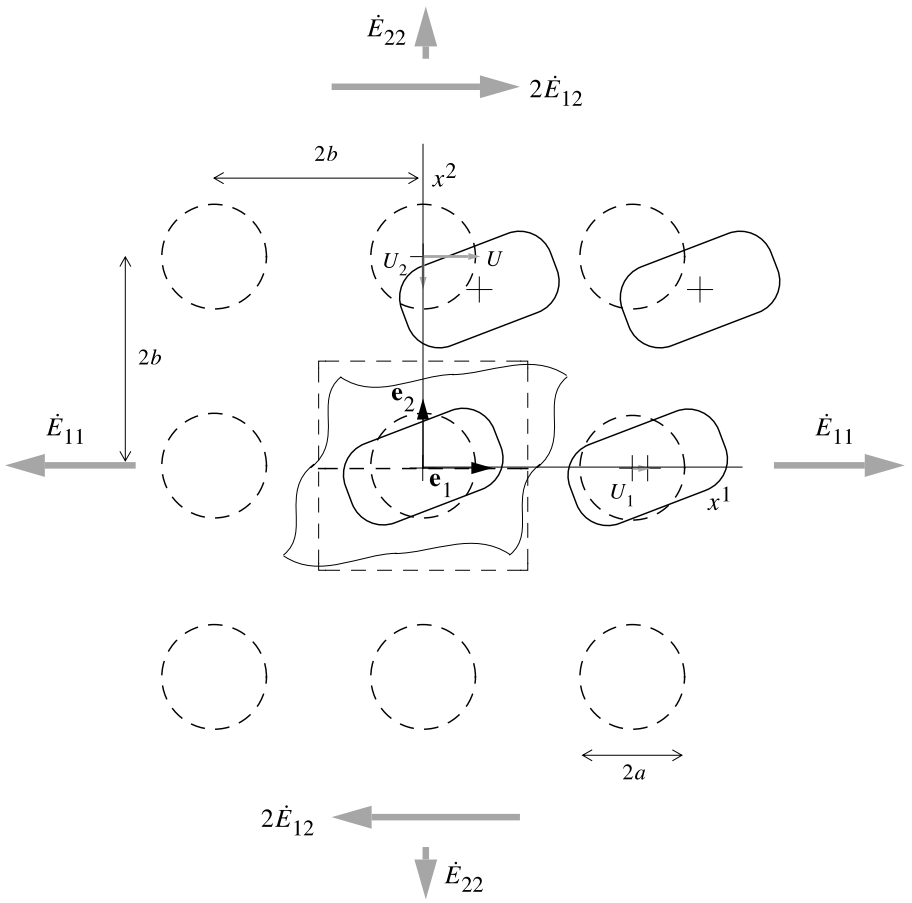

Fig. 1. Sketch of the microstructural model and the remote loading conditions. Dashed lines are used for the undeformed configuration, and part of the deformed configuration is drawn with solid lines. The velocities $\dot{U}$, $\dot{U}_1$ and $\dot{U}_2$ are relative velocities of neighbouring void centres, and are used as degrees of freedom to impose macroscopic deformations $\dot{E}_{ij}$ $(i,j=1,2)$ under full periodic boundary conditions.

boundaries will not remain straight (Fig. 1), as they do in traditional cell analyses of similar problems (Needleman, 1972; Koplik and Needleman, 1988; Sue and Yee, 1988; Steenbrink et al., 1997). Therefore, the solution for this problem requires full periodic boundary conditions. As discussed in detail in Appendix A, the procedure is based on the observation that, because of periodicity, the velocities v_i at two periodic points $x_i^{(a)}$ and $x_i^{(b)}$ under a macroscopic velocity gradient L_{ij} are related by $v_i^{(a)} - v_i^{(b)} = L_{ij}(x_i^{(a)} - x_i^{(b)})$. In addition, since both the void array and the loading conditions preserve point symmetry about the centre of the void, attention can be confined to half of a unit cell.

The problem is analysed using a Total Lagrangian formulation with full account of finite strain effects. Virtual work is expressed as

$$\int_V \tau^{ij}\delta\eta_{ij}\,\mathrm{d}V = \int_S T^i\delta u_i\,\mathrm{d}S \tag{3}$$

with V being the area of the half unit cell in the undeformed reference configuration. As usual, $\delta\eta_{ij}$ is the variation of the Lagrangian strain components associated with the virtual displacements δu_i, τ^{ij} are the components of the second Piola–Kirchhoff stress tensor and T^i are the tractions (all components are with

respect to the undeformed Cartesian base vectors $\mathbf{e}_i$). The boundary S in Eq. (3) comprises effectively only the half void surface contained in the cell, where $T^i = 0$; the cell boundaries are not included because of the periodicity conditions.

The macroscopic Cauchy stresses Σ_{ij} are computed from the forces transmitted through the cell boundaries. These forces are obtained from the tractions T^i in the reference configuration. Thus,

$$\Sigma_{11} = \frac{1}{b(1+E_{22})} \int_0^b T^1(\pm b, x_2)\,\mathrm{d}x_2, \tag{4a}$$

$$\Sigma_{22} = \frac{1}{2b(1+E_{11})} \int_{-b}^b T^2(x_1, \pm b)\,\mathrm{d}x_1, \tag{4b}$$

$$\Sigma_{12} = \Sigma_{21} = \frac{1}{2b(1+E_{22})} \int_{-b}^b T^1(x_1, \pm b)\,\mathrm{d}x_1, \tag{4c}$$

where the factors $1+E_{22}$ or $1+E_{11}$ account for the average change in size of the unit cell in the current deformed configuration. We can write $\pm b$ in the above equations by virtue of equilibrium.

As scalar-valued measures of macroscopic stress and strain we will use

$$\Sigma_{\mathrm{e}} = \frac{\sqrt{3}}{2}\sqrt{(\Sigma_{11}-\Sigma_{22})^2 + 4\Sigma_{12}^2}, \tag{5}$$

$$\Gamma = \sqrt{E_{11}^2 + E_{22}^2 + 2E_{12}^2}. \tag{6}$$

These definitions ensure that Σ_{e} is equal to the macroscopic Von Mises stress, $\Sigma_{\mathrm{e}} = \sqrt{\frac{3}{2}\Sigma'_{ij}\Sigma'_{ij}}$, when the deviator Σ'_{33} in the out-of-plane direction vanishes (as it will during incompressible deformations in plane strain), and Γ is the accumulated shear. The latter is obtained by integration of the macroscopic shear rate

$$\dot{\Gamma} = \sqrt{D_{ij}D_{ij}} = \sqrt{\dot{E}_{11}^2 + \dot{E}_{22}^2 + 2\dot{E}_{12}^2} \tag{7}$$

making use of the fact that $\dot{E}_{ij}$ is constant during the deformation process.

2.2. Constitutive model

The material model taken for the polymer matrix material is a viscoplastic one, which accounts for rate and pressure-dependent yield, strain softening immediately after yield and re-hardening at continued plastic deformation. The three-dimensional (3-D) version of the constitutive equations was first put forward by Boyce et al. (1988), but it is used here in a somewhat different formulation as given by Wu and Van der Giessen (1993, 1996).

The description of yield is based on a constitutive equation for the equivalent plastic shear rate $\dot{\gamma}^{\mathrm{p}}$ originally derived by Argon (1973),

$$\dot{\gamma}^{\mathrm{p}} = \dot{\gamma}_0 \exp\left[-\frac{As_0}{T}\left(1 - \left(\frac{\tau}{s_0}\right)^{5/6}\right)\right]. \tag{8}$$

Here A is a material parameter, T is the absolute temperature and s_0 is the athermal shear strength, and τ is the driving shear stress. Pressure dependence is accounted for by replacing s_0 in Eq. (8) by $s + \alpha p$, with p being a pressure and α, the pressure sensitivity coefficient. Strain softening is modelled phenomenologically by letting s evolve with plastic straining from the initial value s_0 to a steady-state value s_{ss} according to

$$\dot{s} = h\left(1 - \frac{s}{s_{ss}}\right)\dot{\gamma}^{p}. \tag{9}$$

Assuming that the resistance to yield is isotropic, this description is generalized to 3-D states in a J_2-like manner, [1] i.e.

$$\tau = \sqrt{\tfrac{1}{2}\overline{\sigma}'_{ij}\overline{\sigma}'_{ij}}, \qquad \overline{\sigma}_{ij} = \sigma_{ij} - b_{ij}, \tag{10}$$

$$\dot{\gamma}^{p} = \sqrt{d^{p}_{ij}d^{p}_{ij}}, \qquad d^{p}_{ij} = \frac{\dot{\gamma}^{p}}{\sqrt{2}\,\tau}\overline{\sigma}'_{ij}. \tag{11}$$

Here, σ_{ij} are the Cauchy stress components (the $'$ denotes the deviatoric part) and d^{p}_{ij} are the components of the plastic part of the Eulerian strain rates, $d_{ij} = d^{e}_{ij} + d^{p}_{ij}$. The elastic part is taken to be given (under isothermal conditions) by

$$d^{e}_{ij} = \mathscr{L}^{-1}_{ijkl}\overset{\nabla}{\sigma}_{kl} \tag{12}$$

in terms of the Jaumann stress rate $\overset{\nabla}{\sigma}_{kl}$. The elastic properties are also assumed isotropic, so that the moduli $\mathscr{L}_{ijkl}$ can be expressed in the standard way in terms of Young's modulus E and Poisson's ratio v.

The tensor b_{ij} in Eq. (10) is the back stress which is introduced to represent the orientational hardening in amorphous polymers, which is due to the stretching of their network-like molecular structure during plastic flow. The constitutive description of hardening draws on the analogy with the stretching of a cross-linked rubber (Boyce et al., 1988) and is, therefore, based on a specification of the principal back stress components b_α in terms of the principal plastic stretches λ_α. This relationship has been given several times in full details; suffice it here to refer to e.g. Wu and Van der Giessen (1993, 1996). It involves only two additional material parameters, N and C^{R}. The first of these specifies the limit stretch of the molecular chains, while the second parameter is the initial hardening modulus under shear. Although the elastic strains in polymers can be significant, as we shall see later in this paper, we neglect them in computing the plastic stretches needed in the constitutive law for b_{ij}.

The material parameters used in most of the calculations in this paper are taken to be representative of styrene–acrylonitrile (SAN), a typical matrix material for polymer-rubber blends (Steenbrink et al., 1997): $E/s_0 = 12.6$, $v = 0.38$, $s_{ss}/s_0 = 0.79$, $As_0/T = 52.2$, $h/s_0 = 12.6$, $\alpha = 0.25$, $N = 12.0$ and $C^{R}/s_0 = 0.033$. The shear stress response to homogeneous simple shear with these parameters is shown in Fig. 2. This example illustrates the key features of the response in amorphous polymers, especially the softening after yield followed by re-hardening. This feature is responsible for the propagating, localized deformations that will be shown in the next section to control the behaviour of the porous material.

3. Results

3.1. Localized deformations

In this section, we investigate the response of the cavitated (voided) material with the above material characteristics, under different straining triaxialities. The latter are specified through the ratio between the macroscopic strain-rate components $\dot{E}_{ij}$, while the macroscopic shear rate $\dot{\Gamma}$ is equal to $10^{-2}\,s^{-1}$ for all cases. A parametric study of void volume fraction of the blend has been carried out by varying the value of a/b as

[1] Letters in lower case are used for stresses and strain rates at the local scale, i.e. inside the matrix. The corresponding average macroscopic quantities are denoted by capital letters (Eq. (2)).

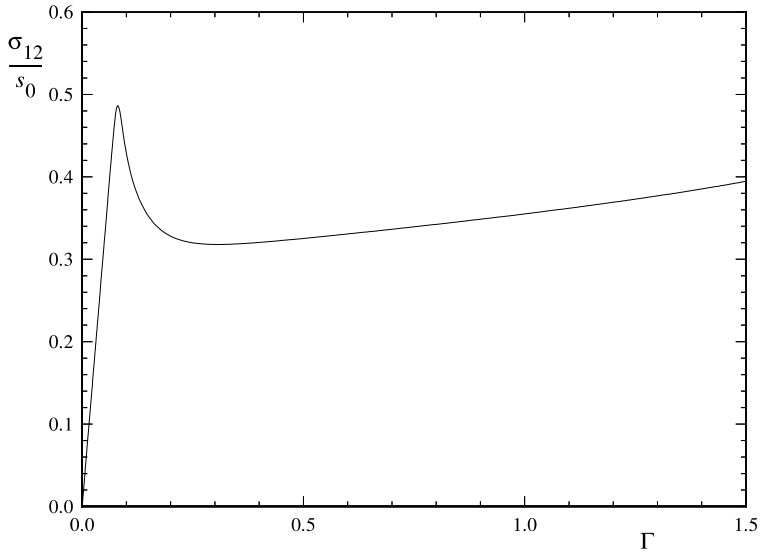

Fig. 2. Shear stress σ_{12} response to homogeneous simple shear Γ at a rate of $\dot{\Gamma} = 10^{-2}\,\mathrm{s}^{-1}$. This is also the macroscopic $\Sigma_e/\sqrt{3}$ vs. Γ curve for homogeneous, unvoided SAN.

0.05, 0.25, 0.5, 0.75 and 0.95, corresponding to void volume fractions of $f = 0.20\%$, 4.9%, 20%, 44% and 71%, respectively.

As expected, the intrinsic softening leads to highly localized deformations in between the voids. A fine mesh of quadrilateral elements, comprising four crossed triangles, is needed to resolve these. The finite element mesh used for voids with $a/b = 0.5$ is shown in Fig. 14 as an example. The localization is most easily seen in contour plots of the plastic shear rate $\dot{\gamma}^p$, which show the locations where momentarily most plastic activity is taking place. As a consequence of the progressive hardening after softening, the shear bands widen (Wu and Van der Giessen, 1996). The associated propagation of the fronts of the shear bands is visualized by the localization of $\dot{\gamma}^p$. Depending on the triaxiality of loading (predominant tension, predominant shearing or a combination of both), different types and directions of shear bands develop.

Under macroscopically simple shear, as shown in Fig. 3, local plastic deformation starts in the form of small 'dog-ear' shear bands (Steenbrink et al., 1998) oriented roughly normal to the maximum principal strain direction. These shear bands propagate with continued macroscopic deformation until new shear bands initiate in between adjacent voids, parallel to the shearing direction. This occurs when the macroscopic yield point is attained, as shown in Fig. 4. Further deformation then localizes in these shear bands, as evidenced by macroscopic softening. Once the ligaments between adjacent particles/voids are completely crossed by shear bands, large deformations on a macroscopic scale are possible. Continued macroscopic straining is accommodated by widening of the shear bands, as shown in the last snapshot in Fig. 3, at roughly constant macroscopic shear stress (Fig. 4). Note the severe distortion of the void shapes, which was demonstrated first by Pijnenburg et al. (1999), as well as the distortions of the unit cell. They once again demonstrate the absence of the constraints that were implied by the previous, more traditional cell analyses of Steenbrink et al. (1997, 1998) under high-symmetry loading conditions.

Although the details can be quite different, similar patterns of deformation as seen in Figs. 3 and 4 are found under different macroscopic straining conditions. As examples, Figs. 5 and 6 show snapshots of the distribution of plastic shear rate under plane strain tension and under biaxial tension in combination with shear, respectively. Due to the symmetry in morphology and loading, the unit cell does not change shape under tension and the results in Fig. 5 are fully similar to those presented by Steenbrink et al. (1998).

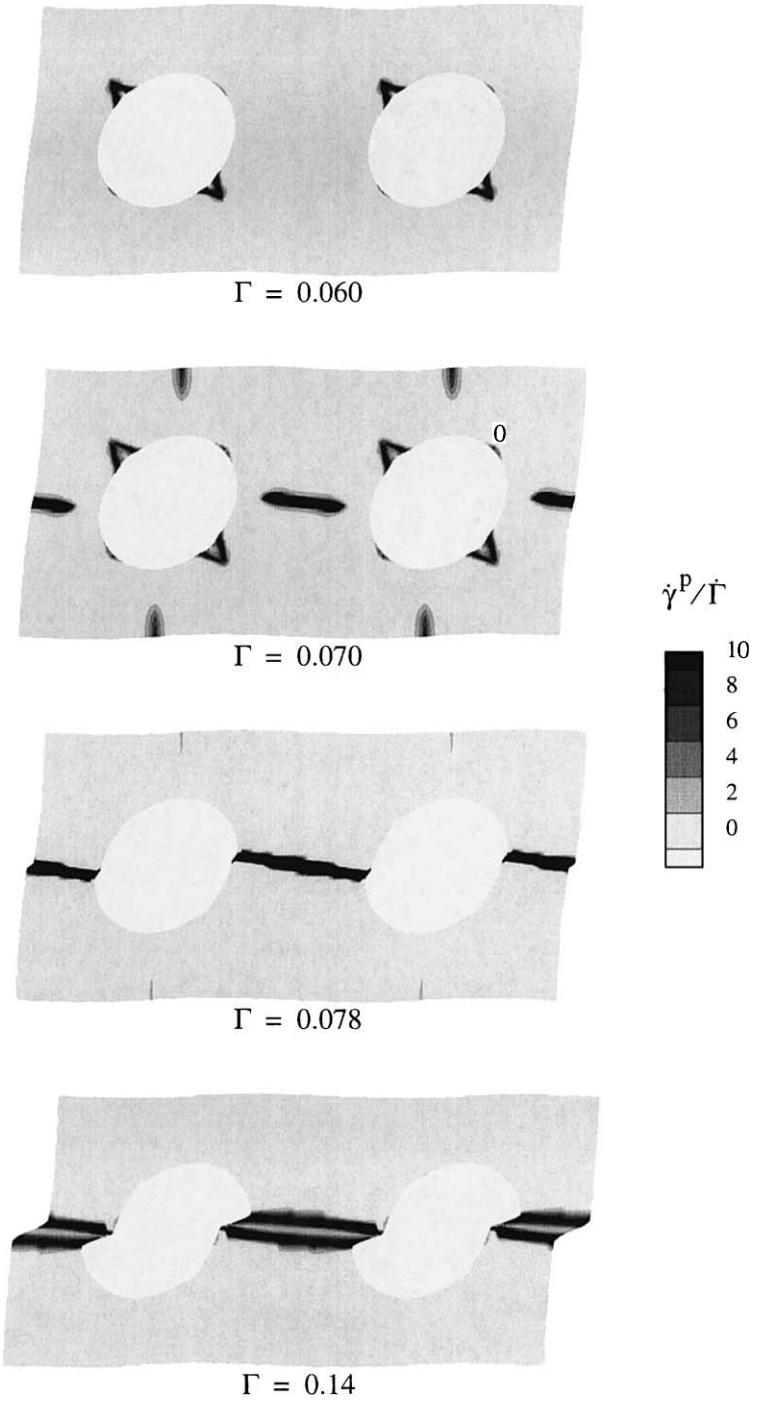

Fig. 3. Distribution of instantaneous plastic shear rate $\dot{\gamma}^p$, normalized by the macroscopic shear rate $\dot{\Gamma}$, at four stages of the deformation. The applied loading is simple shear, $\dot{E}_{12} = \dot{\Gamma}/\sqrt{2}$. The corresponding stress–strain curve, with indication of the snapshots, is shown in Fig. 4.

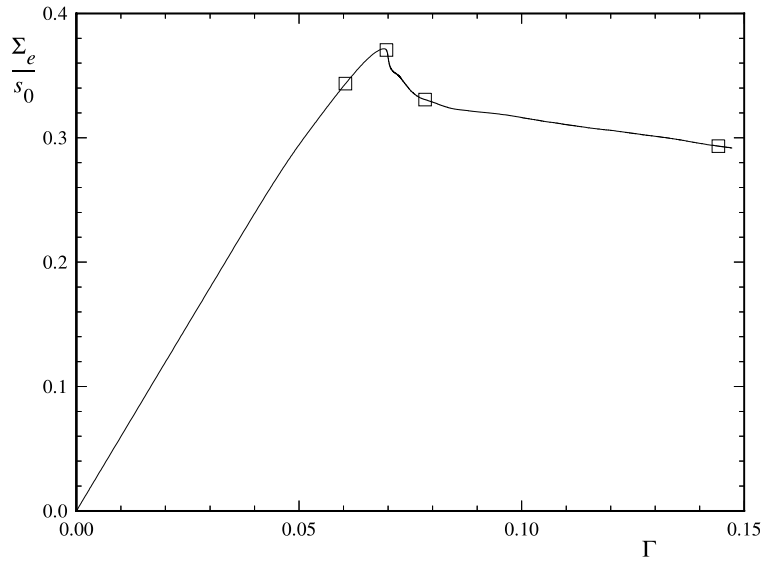

Fig. 4. Macroscopic shear stress ($\Sigma_{12} = \Sigma_e/\sqrt{3}$) response to simple shear, i.e. $\Gamma = \sqrt{2}E_{12}$, for SAN with $a/b = 0.5$. The square symbol refer to the four snapshots in Fig. 3.

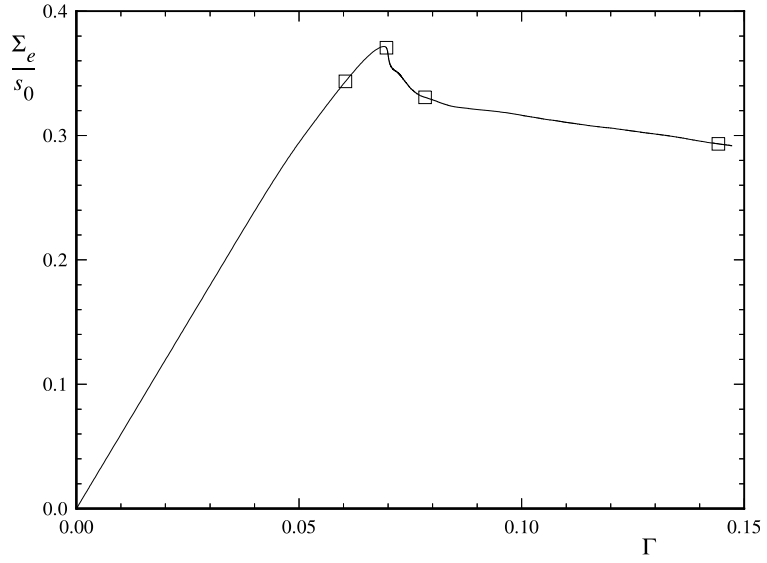

Fig. 5. Distribution of instantaneous plastic shear rate $\dot{\gamma}^p$ at four stages of deformation. Applied loading: plane strain tension, $\dot{E}_{11} = \dot{\Gamma}$. As in Fig. 3, the four snapshots are taken just before; almost at; just after and far away from macroscopic yield.

Many more different straining conditions have been analysed (not shown), and in all instances we first observe some plastic activity around the void. This initial plasticity tends to occur in shear bands that closely resemble 'dog-ear' shear bands (second snapshots in Figs. 5 and 6). Upon further macroscopic deformation, the effective stress attains a maximum at the instant that shear bands are crossing the ligament between the voids. Then, the material softens and larger deformations are possible (third snapshots

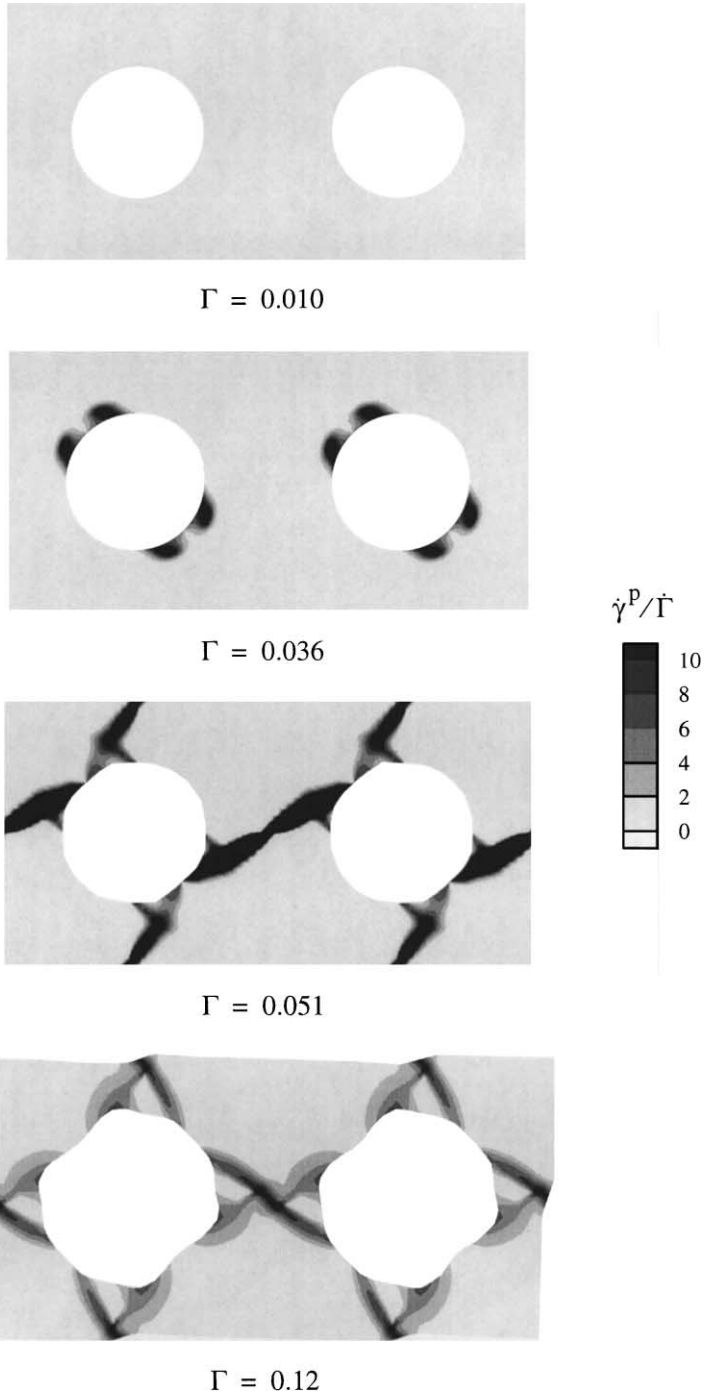

Fig. 6. Distribution of instantaneous plastic shear rate $\dot{\gamma}^p$ at four stages of deformation. Applied loading: biaxial tension in combination with simple shear, $\dot{E}_{11} = \dot{E}_{22} = 2\dot{E}_{12} = \sqrt{2/5}\dot{\Gamma}$. As in Fig. 3, the four snapshots are taken just before; almost at; just after and far away from macroscopic yield.

in Figs. 3, 5 and 6). With continued straining, the material in the original shear band in between neighbouring voids locks, and subsequently the shear band propagates through the matrix material in a variety of ways depending on the macroscopic triaxiality.

3.2. Macroscopic yield

The macroscopic responses in the different straining conditions have qualitatively the same characteristics as the one shown in Fig. 4, with a distinct maximum effective stress level. Although the response is intrinsically rate dependent, the macroscopic yield stresses under different triaxialities may be compared, since all computations have been carried out for the same value of the macroscopic shear rate $\dot{\Gamma}$. If the voided material (or a representative volume element of this material) is macroscopically isotropic, macroscopic yield can be fully characterized by the macroscopic stress invariants Σ_m, Σ_e and a similarly defined third invariant (which is usually less relevant). The square array of voids considered here (Fig. 1) implies a material which is not isotropic. Nevertheless, as a first approximation and in view of the Gurson yield formulation, we investigate the instants of macroscopic yield in Σ_e vs Σ_m stress space for the various deformation triaxialities.

The results of numerous cell computations at different ratios of $\dot{E}_{ij}/\dot{\Gamma}$ for three void volume fractions are summarized in Fig. 7. For each volume fraction, there is some scatter in the various yield points for different triaxialities, but in the regime where $\Sigma_m > 0$, most points seem to lie on a single envelop. At stress triaxialities Σ_m/Σ_e around 1, some points would fall outside this envelop. This must be attributed to the fact that with the three degrees of freedom in the present cell calculations (Fig. 1), there are various combinations of $\dot{E}_{ij}/\dot{\Gamma}$ that lead to nearly the same stress triaxialities but different stress levels.

Another interesting observation from Fig. 7 is that there can be very significant variations in yield stress for almost the same value of Σ_m/Σ_e in the regime of slightly negative stress triaxialities. In fact, the highlighted results are for one of the loading cases

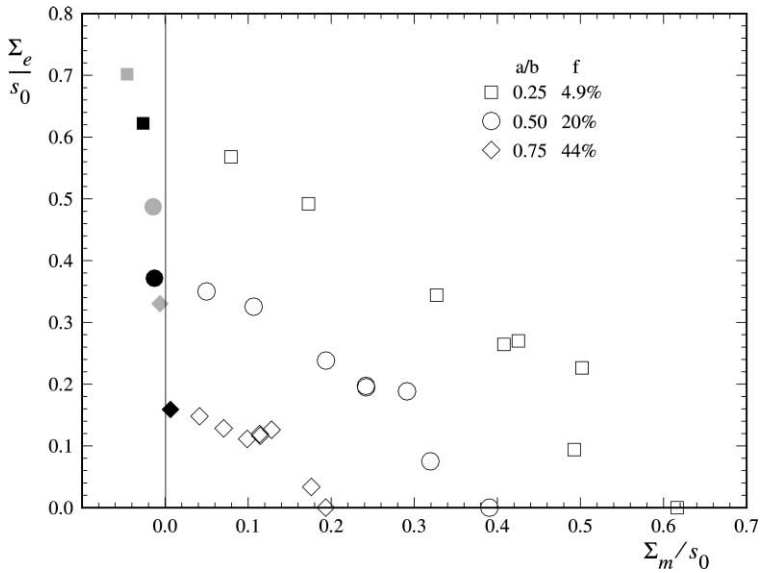

Fig. 7. Location of the yield points in Σ_e–Σ_m space for various void volume fractions. The black symbols indicate results for simple shear, the grey symbols identify pure shear.

$$\text{Simple shear} \quad L_{ij} = \frac{1}{\sqrt{2}} \begin{pmatrix} 0 & 2\dot{\Gamma} \\ 0 & 0 \end{pmatrix}, \tag{13}$$

$$\text{Pure shear} \quad L_{ij} = \frac{1}{\sqrt{2}} \begin{pmatrix} \dot{\Gamma} & 0 \\ 0 & -\dot{\Gamma} \end{pmatrix}, \tag{14}$$

with pure shear requiring consistently higher yield stresses. The simple explanation for this is that under pure shear according to Eq. (14), the actual shearing takes place at an angle of 45° to the simple shear ($\mathbf{e}_1$) direction (neglecting finite strains). In this direction, the ligament between the voids is $\sqrt{2}$ times as large (Fig. 1), which has a big effect on the macroscopic yielding of the material, since we have seen in the previous section that this involves shear yielding of the ligament.

In fact, we can readily estimate this effect for a rate independent material by a simple argument previously used in the work of Pijnenburg et al. (1999). Consider simple shear at the moment of macroscopic yielding when virtually all plastic deformation is taking place in the narrowest section between voids (Fig. 3). Equilibrium requires that the shear force at the top of the cell, $f_{\text{top}} = 2b\Sigma_{12}$, equals that on the ligament of width $2(b-a)$, $f_{\text{lig}} = 2(b-a)\tau_{\text{lig}}$. At yield, τ_{lig} is equal to the shear yield strength τ_{y} of the matrix material, so that we obtain

$$\Sigma_{12} = (1 - a/b)\tau_{\text{y}}. \tag{15}$$

From this, we see that the macroscopic yield stress is directly proportional to the relative size of the ligament, $1 - a/b$. Since the ligament width in the direction of pure shear is $\sqrt{2}$ times larger, we expect that the yield stress under pure shear is correspondingly higher than in simple shear. The data in Fig. 7 are consistent with this. As a further test, we repeated the simple shear calculations for $a/b = 0.25$, 0.5 and 0.75 with a $\sqrt{2}$ times smaller a. The values of the effective yield stress were found to be $\Sigma_{\text{e}}/s_0 = 0.68$, 0.52 and 0.34. These agree well with macroscopic yield stresses under pure shear, with values $\Sigma_{\text{e}}/s_0 = 0.70$, 0.49 and 0.33, thus confirming the accuracy of estimate (15).

A final remark about the shear data points is that the Σ_{m} value at maximum Σ_{e} is not zero as one would expect. This is due to the fact that the computations are strain controlled and not stress controlled. This implies that the macroscopic stressing is not proportional and that the stress triaxiality is not constant. However, the stress trajectories in Σ_{e}–Σ_{m} space depicted in Fig. 8 show that the deviations from proportionality remain quite small.

4. Macroscopic constitutive model

4.1. Yield potential

Steenbrink et al. (1997) formulated a 3-D (axisymmetric) viscoplastic model for the macroscopic response of a voided polymer by using Gurson's yield function. Here we formulate the corresponding plane strain version in a completely similar fashion. Based on Gurson's planar yield function (but in terms of an effective shear stress rather than a Mises effective stress), we start by introducing the function

$$\Phi = C_{\text{e}} \frac{1}{2} \frac{\overline{\Sigma}'_{ij}\overline{\Sigma}'_{ij}}{\tau^2} + 2f \cosh\left(\frac{\Sigma_{\text{m}}}{\tau}\right) - 1 - f^2 = 0, \quad C_{\text{e}} = (1 + 3f + 24f^6)^2 \tag{16}$$

in terms of the macroscopic Cauchy stress Σ_{ij}. The coefficient $C_{\text{e}}(f)$ is an empirical factor introduced by Gurson (1977) for plastic flow under plane strain conditions. The function Φ serves as a potential for the plastic part D^{p}_{ij} of the macroscopic strain rate D_{ij} according to

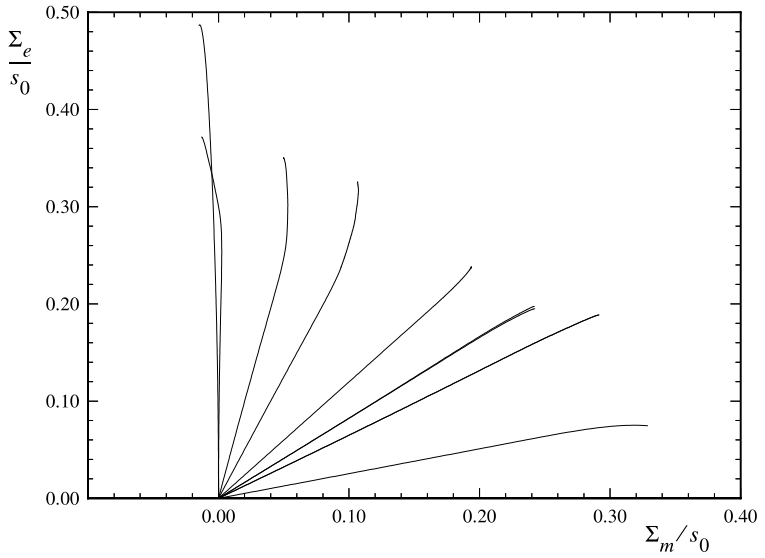

Fig. 8. Trajectories in Σ_e–Σ_m space for cell calculations for $a/b = 0.5$ under different applied deformation triaxialities. The endpoints of the curves correspond to the macroscopic yield points in Fig. 7.

$$D_{ij}^{p} = \dot{\Lambda}\frac{\partial \Phi}{\partial \overline{\Sigma}_{ij}}, \tag{17}$$

where $\dot{\Lambda}$ is obtained from the condition that the plastic work rate in the porous material per unit volume, $\overline{\Sigma}_{ij}D_{ij}^{p}$, be equal to the dissipation in the matrix material, i.e.

$$\overline{\Sigma}_{ij}D_{ij}^{p} = (1-f)\sqrt{2}\,\tau\dot{\gamma}^{p}. \tag{18}$$

The function Φ also serves to provide the driving stress τ for the given stress state (including the current back stress state) by solution from the condition $\Phi = 0$ in Eq. (16). This τ is to be substituted into Eq. (8) in order to obtain the effective shear rate $\dot{\gamma}^{p}$ to be used in Eq. (18). For $f = 0$, τ from Eq. (16) reduces to Eq. (10), and the flow rule (17) reduces to Eq. (11), both for the corresponding macroscopic quantities.

Fig. 9 shows the macroscopic yield curve according to Eq. (16) for the same three values of a/b as in Fig. 7, using $f = (\pi/4)(a/b)^2$. The macroscopic yield surface is obtained from the above viscoplastic model under constant stress triaxiality in an approximate manner by arguing that macroscopic yield takes place at a maximum of the effective stress, so that the elastic shear rate vanishes at yield. Thus, we set $\dot{\gamma}^{p}$ equal to the applied shear rate $\dot{\Gamma}$, determine the required value of τ from Eq. (8) and obtain the yield stress from Eq. (16) under the assumption of proportional stressing (the back stress still vanishes at the initiation of yield) and by neglecting void growth during elastic loading. Also shown in Fig. 9 are the cell results from Fig. 7, and it is clearly seen that Eq. (16) significantly overestimates these results for all void fractions and over the entire range of triaxialities Σ_m/Σ_e.

Recalling the deformation patterns discussed in the previous section, we argue that these differences at low triaxialities are caused by the fact that plastic flow in the voided polymer occurs by highly localized deformations. Gurson derived his potential primarily for metals, which do not exhibit the softening after yield so that plasticity is more confined in a diffuse region around each void (Koplik and Needleman, 1988). As a consequence, yield under (simple or pure) shear conditions (e.g. $\Sigma_{11} = \Sigma_{22} = 0$) occurs when

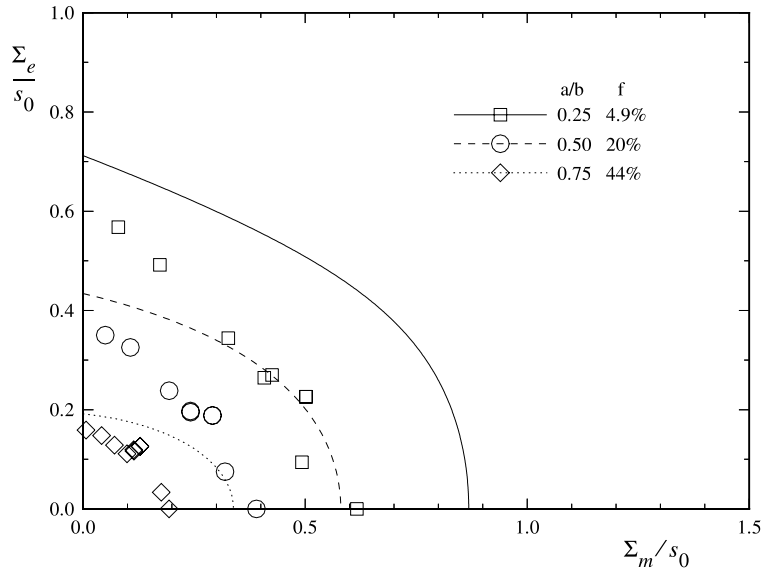

Fig. 9. Comparison of the macroscopic yield surfaces according to the original Gurson potential (16) and the results of the cell analyses from Fig. 7 at the same value of $\dot{\Gamma}$ and the same matrix properties.

$$\Sigma_{12} = \frac{(1-f)}{\sqrt{C_e(f)}}\tau \tag{19}$$

according to Eq. (16). However, as demonstrated in Section 3.2, shear banding occurs in polymers preferentially in the ligaments between voids. Under shear, this leads directly to the yield condition (15), which can be rewritten in terms of f as

$$\Sigma_{12} = (1 - 2\sqrt{f/\pi})\tau. \tag{20}$$

Ligament shearing is controlled by the void volume fraction through $\sqrt{f}$, whereas according to Eq. (19), it is controlled by f.

The distinct deviation from Gurson's prediction of the yield stress at high triaxialities was also observed by Steenbrink et al. (1997) under the axisymmetric stressing conditions that they considered. They have investigated the cause for this in terms of an analysis of a spherical void in a spherical matrix under purely hydrostatic loading, and found that finite elasticity effects play a pivotal role. Furthermore, they were able to formulate a modification of the Gurson potential that agreed better with their axisymmetric cell calculations. In Appendix B, we repeat their analysis for the present case of cylindrical voids under plane strain and find that yield under purely hydrostatic loading occurs when

$$\operatorname{arccosh}\left(\frac{1+\Lambda_f^2}{2\Lambda_f}\right) = \frac{e}{2}\ln\left(\frac{\Sigma_m}{e\tau}+1\right), \quad e = \frac{5}{4}\left[\ln\left(3\frac{\tau}{E}\right)-1\right] \tag{21}$$

with $\Lambda_f = a/b$. The factor e, as defined in the last equality, incorporates the effect of finite elastic strains; the coefficient $5/4$ is a fit to numerical results. When elasticity can be neglected, i.e. $\tau \ll E$, we have $e \to -\infty$ and Eq. (21) reduces to the same condition as obtained from Eq. (16) under pure hydrostatic stressing, i.e. $\overline{\Sigma}'_{ij}\overline{\Sigma}'_{ij} = 0$ (Appendix B).

Expressions Eqs. (21) and (20) embody modifications of the Gurson potential in two extreme cases, $\Sigma_e = 0$ and $\Sigma_m = 0$, respectively. Recognizing that $\Lambda_f = a/b$ in Eq. (21) is equal to $2\sqrt{f/\pi}$ for the square

array of voids assumed in Fig. 1, we now propose to combine the two extreme cases in the form of the following potential for the voided polymer

$$\Phi = \frac{1}{2}\frac{\overline{\Sigma}'_{ij}\overline{\Sigma}'_{ij}}{\tau^2} + 2\Lambda_f \cosh\left[\frac{e}{2}\ln\left(\frac{\Sigma_{\mathrm{m}}}{e\tau}+1\right)\right] - 1 - \Lambda_f^2 = 0. \tag{22}$$

Formally, there is no basis for this expression, but it retains the structure of the Gurson potential (16) while it reduces to Eqs. (21) and (20) under purely hydrostatic conditions and under shear of a square cell, respectively.

In formulating Eq. (22), we have chosen to use Λ_f as a ligament parameter for incorporating the effect of porosity on yield. It emphasizes the importance of the relative ligament size rather than the void volume fraction f, but can be expressed in terms of the latter. There is some ambiguity in this, however. For a void in a square unit cell, $\Lambda_f = a/b = 2\sqrt{f/\pi}$, but for a void in a circular cell (as used in Appendix B), the void volume fraction would just be equal to $(a/b)^2$ so that $\Lambda_f = \sqrt{f}$. This expresses that the ordering of voids becomes important when ligament shearing is the key mechanism at yield. Evidently, in a real blend with a random packing of rubber particles, shear bands will occur in different ligament orientations at various locations in the material. Thus, the most appropriate value of Λ_f will probably depend on the loading direction and the disorder in the packing.

Fig. 10 compares the yield surfaces in Σ_{e}–Σ_{m} space according to Eqs. (16) and (22) and $\Lambda_f = 2\sqrt{f/\pi}$ with the results of the cell calculations. The results presented in this figure are for a matrix material that is not pressure sensitive, i.e. $\alpha = 0$, in order to enable a clear comparison. This figure once again demonstrates that Eq. (16) does not display the correct dependence on f. For low void volume fractions ($f = 4.9\%$), the original Gurson potential (16) overestimates the yield point, while for high volume fractions ($f = 44\%$) it underestimates yield. By virtue of the construction of the modified potential (22), the agreement with the cell analyses is excellent for $\Sigma_{\mathrm{e}} \approx 0$ and $\Sigma_{\mathrm{m}} \approx 0$. For intermediate triaxialities, the numerical cell results are not captured with the same accuracy, but the agreement is much better than with the original potential (16).

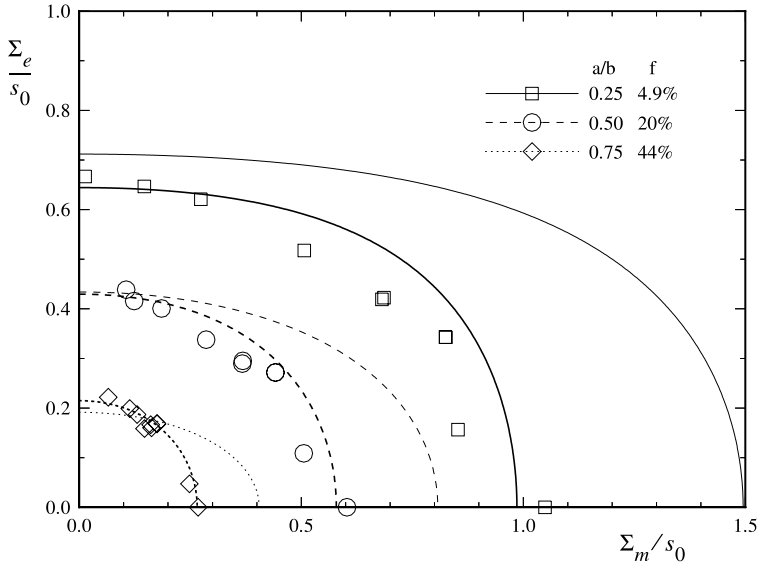

Fig. 10. Comparison of the macroscopic yield surfaces as predicted by the original Gurson potential (16) (thin curves), the modified potential (22) with $\Lambda_f = 2\sqrt{f/\pi}$ (thick curves) and the finite element cell calculations for $\alpha = 0$, i.e. no pressure dependence. The other matrix properties and the applied loading rate $\dot{\Gamma}$ are the same as in Fig. 7.

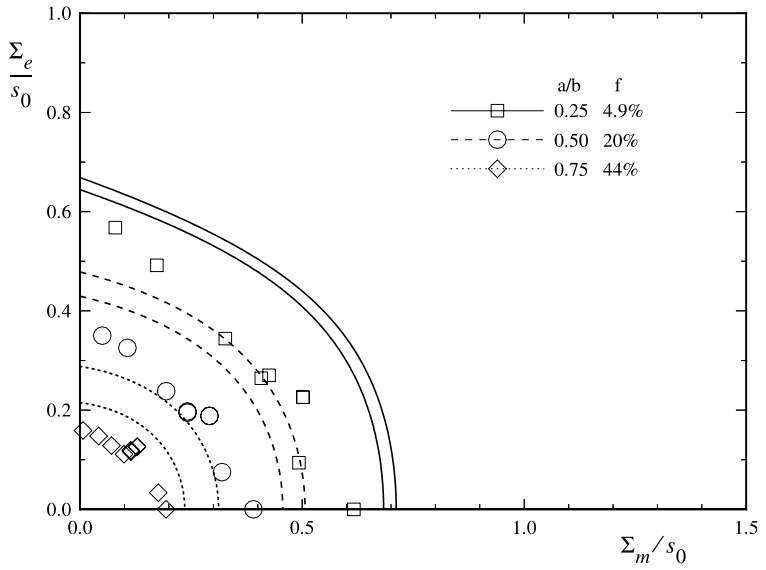

Fig. 11. Comparison of the macroscopic yield surfaces according to the modified Gurson model of Eq. (22) and the results of the cell analyses from Fig. 7. For each a/b, two curves according to Eq. (22) are shown: the lower one is for $\Lambda_f = 2\sqrt{f/\pi}$ and the upper one corresponds to $\Lambda_f = \sqrt{f}$. The matrix properties and the applied loading rate $\dot{\Gamma}$ are the same as in Fig. 7.

When pressure dependent yield in the matrix is accounted for, as shown in Fig. 11, the agreement between potential and cell results is somewhat less. The reason for this is that the potential does not account for pressure effects on yield in the local scale in between the voids in the blend. The importance of these local hydrostatic stresses can be estimated from the shear results. Macroscopically, shear would give no hydrostatic stress, so that along the Σ_e axis the results with or without pressure dependence should be the same. Inspection of the cell results in Figs. 10 and 11 reveals that this is not the case; local pressures clearly have a substantial influence on the macroscopic yield, even at $\Sigma_m = 0$.

The yield surface according to Eq. (22) is plotted twice in Fig. 11; the second time by replacing $\Lambda_f = 2\sqrt{f/\pi}$ with $\Lambda_f = \sqrt{f}$. The reason for showing this is to give an indication of the sensitivity of the results on the value of Λ_f in Eq. (22). As mentioned before, the exact expression for Λ_f will not only depend on f, but also on the particle (size) distribution and loading direction. However, from the two models considered, we may draw the important conclusion that the influence of the void volume fraction goes as $\sqrt{f}$ rather than f as in the Gurson model. While fine tuning with a prefactor may improve the results even further, the biggest gain in accuracy is made with that crucial observation.

4.2. Elastic–viscoplastic constitutive model

The theory for macroscopic plastic flow outlined above is complemented in the usual way (Koplik and Needleman, 1988; Steenbrink et al., 1997) with the void evolution relation

$$\dot{f} = (1 - f)D_{kk}. \tag{23}$$

Macroscopic elasticity is described by the same type of expression as Eq. (12) but with the macroscopic elastic moduli dependent on f. According to Zhao et al. (1989) and Christensen (1979), a random packing of parallel cylindrical voids in a matrix leads, using Mori-Tanaka's mean field theory and Eshelby's solution,

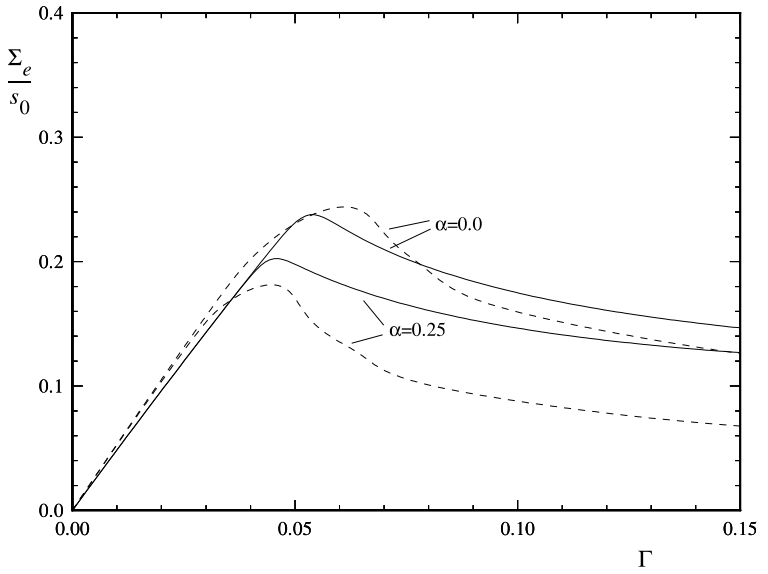

Fig. 12. Stress–strain response to plane strain tension ($\dot{E}_{11} = \dot{\Gamma}$) according to the finite element cell calculations (- - -) and to the macroscopic elastic–viscoplastic relation (—) based on the modified Gurson potential (22) (Section 4.2).

to overall isotropic properties in the plane normal to the cylinders with Young's modulus E^* and Poisson's ratio v^* given by

$$E^* = \frac{(1-f)E}{1+2f(1-v^2)}, \qquad v^* = \frac{(1-f)v + f(1-2v^2)}{1+2f(1-v^2)} \tag{24}$$

in terms of the matrix properties E and v. These can then be used for the macroscopic elasticity properties for the plane strain model considered here (Fig. 1), ignoring the influence of the regular void packing for simplicity.

The stress–strain curve for plane strain tension, calculated with Eq. (22) and these moduli is shown in Fig. 12. The agreement with the cell calculations is reasonable, especially when there is no pressure dependence. Here, again the local pressures in the cell results cause a larger deviation from the predictions of the potential. We also see that the initial slope of the curve, determined by Eq. (24), agrees well with the numerical calculations.

5. Three-dimensional generalization

It is rather straightforward to generalize the foregoing discussion to a real 3-D model, where the voids are no longer cylindrical but spherical with radius a and linear half spacing b. In three dimensions, the original Gurson yield function adapted to a potential for porous polymers (Steenbrink et al., 1997) reads

$$\Phi = \frac{1}{2}\frac{\overline{\Sigma}'_{ij}\overline{\Sigma}'_{ij}}{\tau^2} + 2f\cosh\left(\frac{\sqrt{3}}{2}\frac{\Sigma_{\mathrm{m}}}{\tau}\right) - 1 - f^2 = 0. \tag{25}$$

The modification of the potential in this case is still made up of two separate elements.

First, we consider the effect of localized shearing. A similar analysis of simple shear as that in Section 3.2 but now for a spherical void of radius a in a cubic cell with sides $2b$ shows that the average shear stress in the ligament, τ, is related to the macroscopic shear stress Σ_{12} through f according to

$$\Sigma_{12} = \left(1 - \frac{\pi}{4}\left(\frac{6f}{\pi}\right)^{2/3}\right)\tau \tag{26}$$

with $f = (\pi/6)(a/b)^3$. Evidently, different 3-D packings of voids may lead to slightly different results. For instance, for a spherical void in a spherical matrix, the 3-D generalization of the cylindrical model would lead to $\Lambda_f = (a/b)^2 = f^{2/3}$. At any rate, the key observation is that the shear yield stress is proportional to $f^{2/3}$ rather than f as implied by Eq. (25). Next, we have to include elastic effects under high triaxiality stress states. This modification has been analysed in detail by Steenbrink et al. (1997), and can be directly applied here. We then arrive at the 3-D modified Gurson potential

$$\Phi = \frac{1}{2}\frac{\overline{\Sigma}'_{ij}\overline{\Sigma}'_{ij}}{\tau^2} + 2\Lambda_f \cosh\left[\frac{2}{3}e\ln\left(\frac{1}{e}\frac{\sqrt{3}}{2}\frac{\Sigma_{\mathrm{m}}}{\tau} + 1\right)\right] - 1 - \Lambda_f^2 = 0 \tag{27}$$

with e in the 3-D case given by

$$e = \ln\left(\frac{3\sqrt{3}}{2}\frac{\tau}{E}\right) - 1 \approx \ln\left(\frac{\tau}{E}\right). \tag{28}$$

The factor $2/3$ in front of the parameter e is not present in the formulation of Steenbrink et al. (1997) and is merely a result of the different dependence on f.

The constitutive theory is completed by the same void evolution relations (23) as in two dimensions. Finally, Steenbrink et al. (1997) estimated the elastic moduli of the porous material by

$$E^* = \frac{2E(7-5\nu)(1-f)}{2(7-5\nu) + (1+\nu)(13-15\nu)f}, \tag{29}$$

$$\nu^* = \frac{2\nu(7-5\nu) + (1+\nu)(3-5\nu)f}{2(7-5\nu) + (1+\nu)(13-15\nu)f} \tag{30}$$

based on work of Jeong and Pan (1995) and Tandon and Weng (1988).

By construction, Gurson's equation (25) is in fact an upper bound to the yield surface in a rigid perfectly plastic, porous solid. Sun and Wang (1989) were able to find an expression for the lower bound of the yield surface, which takes the form (for $f \leqslant 0.3$)

$$\Phi = \frac{1}{3}\left(\frac{\Sigma_{\mathrm{e}}}{\tau}\right)^2 + f\frac{\beta_2 \cosh\left(\frac{q}{\sqrt{3}}\frac{\Sigma_{\mathrm{m}}}{\tau}\right)}{\left[1 + \beta_4 f^2 \sinh^2\left(\frac{q}{\sqrt{3}}\frac{\Sigma_{\mathrm{m}}}{\tau}\right)\right]^{1/2}} - \beta_3 = 0 \tag{31}$$

with

$$q = \tfrac{3}{2}, \quad \beta_2 = 2 - \tfrac{1}{2}\ln f, \quad \beta_3 = 1 + f(1 + \ln f),$$

$$\beta_4 = \left(\frac{\beta_2}{\beta_3}\right)^2 \coth^2\left(\frac{q}{\sqrt{3}}\frac{\Sigma_{\mathrm{m}}^0}{\tau}\right) - \left[f^2 \sinh\left(\frac{q}{\sqrt{3}}\frac{\Sigma_{\mathrm{m}}^0}{\tau}\right)\right]^{-1}$$

and

$$\Sigma_{\mathrm{m}}^0 = -0.65\sqrt{3}\tau\ln f.$$

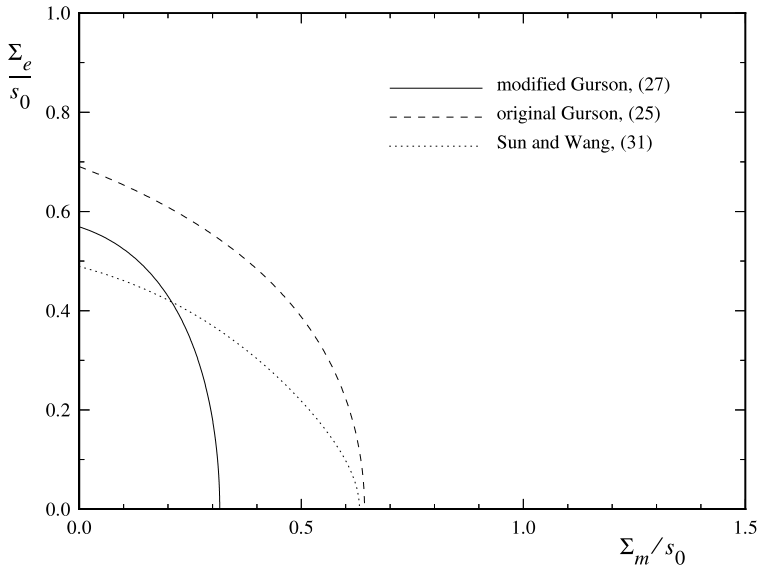

Fig. 13. Macroscopic yield surfaces for porous polymers ($f = 0.20$) according to three 3-D yield potentials (25), (31) and (27). The latter uses $\Lambda_f = f^{2/3}$.

Fig. 13 shows the prediction of the yield curves by all three potentials (25), (27) and (31), for a volume fraction $f = 0.20$, which is a typical value of the volume fraction of rubber in practical blends, and $\Lambda_f = f^{2/3}$. We see that along the Σ_{m} axis, the upper and lower bound for the perfectly plastic material do not differ much. Including elasticity effects under high triaxiality, yields a much more substantial shift of the yield curve. On the Σ_{e} axis, there is a difference between Eqs. (25) and (31) for the volume fraction considered here. The prediction of Eq. (27) is somewhere in between, but the dependence of Eqs. (25) and (31) on f is quite different from that of Eq. (27).

6. Conclusion

The cell calculations presented in this paper show that the standard Gurson (1977) formulation for voided materials has limited applicability to porous polymers for two reasons: the contribution of elastic deformations and the localized nature of plastic deformation. Elasticity effects have a significant influence on the yield surface under hydrostatic loading, while localization into shear bands in polymers results in a different dependence on the void volume fraction than in the standard formulation. Both effects tend to move the yield surface to lower values in stress space, so that Gurson's theory tends to overestimate the real macroscopic yield surface. The two reasons are directly related to key characteristics of the response of polymers that are distinctly different from that of metals for which Gurson (1977) originally developed the yield surface.

The plane strain modified yield potential (for rate-dependent flow) that we propose here depends on the porosity not through the void volume fraction f, but through the relative dimension of the ligament which scales as $\sqrt{f}$. This is a consequence of the localization of plastic flow in the ligament at macroscopic yield. The localization of plastic deformation around the voids has been studied before by Steenbrink et al. (1997, 1998), Steenbrink and Van der Giessen (1999) but there this phenomenon had not been so clearly found. The reason for this is that these previous studies have used the more or less standard unit cell calculations

(Koplik and Needleman, 1988) where the material is subjected to a macroscopic principal stress state. The resulting deformations around the voids are then constrained to the symmetries implied by such unit cells. The presence of a shear component would break this symmetry. A unit cell analysis then requires full periodic boundary conditions to avoid any constraints. Then, as we have shown here, the intrinsic tendency for strain localization in amorphous polymers leads to a strong preference for plastic shearing of the ligament between voids.

It is worth noting that cell analyses under non-principal stress states are straightforward in 2-D, but cannot be done in the axisymmetric approximations that are frequently used for 3-D cells. Then, one needs to resort to truly 3-D cell analyses in order to correctly study the plastic flow localization in between neighbouring voids without any artificial symmetry constraints. Socrate and Boyce (2000) have also recently emphasized the artifacts that may result from the constraints in the traditional axisymmetric cell analyses for voided polymers.

The dependence of the overall yield potential on $\sqrt{f}$ differs fundamentally from the work of Gurson (1977) and others since then. For instance, the introduction of extra q factors, as has been done by Tvergaard (1981, 1982), only serves to scale the dependence on f. The primary cause for this difference lies in the strong initial hardening in metals which prevents localization, so that plastic flow around the voids is still rather confined at the onset of macroscopic yield. It is only in the stage of void coalescence that plastic deformations localize in the ligament. This stage has been studied quite intensively e.g. by Leblond and Perrin (1991), Richelsen and Tvergaard (1994), and very recently by Pardoen and Hutchinson (1999), who have explicitly emphasized the localization of flow in the ligament. Qualitatively, our present results can be reconciled with these by noting that, due to the intrinsic tendency for localization in amorphous polymers, the onset of macroscopic yield more or less coincides with void coalescence.

The dependence of macroscopic yield in polymers on the void volume fraction through the relative ligament size evidently relies on the assumption of a periodic packing of the void or cavitated particles. The localized deformation patterns in a randomly voided polymer will be very complex, as demonstrated by the 2-D simulations of Smit et al. (1999). For such realistic cases, it is not obvious which appropriate average characteristic of the void distribution controls the macroscopic yield in such a case. This is an issue that requires further study.

Appendix A

This appendix describes how to set up the proper periodic boundary conditions that incorporate the macroscopic loading according to Eq. (1). First, we recall that if the material would be homogeneous (no voids), the velocity $\mathbf{v}$ at two points $\mathbf{x}_a$ and $\mathbf{x}_b$ ($\Delta\mathbf{x} = \mathbf{x}_a - \mathbf{x}_b$) under a macroscopically homogeneous velocity gradient $\mathbf{L}$ are related by $\mathbf{v}(\mathbf{x}_a) - \mathbf{v}(\mathbf{x}_b) = \mathbf{L} \cdot \Delta\mathbf{x}$. This relation holds also for inhomogeneous yet periodic fields if $\mathbf{x}_a$ and $\mathbf{x}_b$ are periodic as well. Such relationships have been employed to formulate the proper boundary conditions (Fig. 1). Due to the symmetry of the cell and the symmetry of the applied principal strain rates and the antisymmetry of the shear rate, it suffices to analyse half of the cell. When we take the origin at the centre of the void in our cell, we can write the boundary and periodicity conditions in undeformed coordinates as (with $\dot{U}_1 = 2b\dot{E}_{11}$, $\dot{U}_2 = 2b\dot{E}_{22}$ and $\dot{U} = 2b\dot{E}_{12}$)

$$\dot{\mathbf{u}}(0, b) = \tfrac{1}{2}\dot{U}\mathbf{e}_1 + \tfrac{1}{2}\dot{U}_2\mathbf{e}_2, \tag{A.1a}$$

$$\dot{\mathbf{u}}(-x_1, b) = -\dot{\mathbf{u}}(x_1, b) + \dot{U}\mathbf{e}_1 + \dot{U}_2\mathbf{e}_2, \tag{A.1b}$$

$$\dot{\mathbf{u}}(\pm b, b) = \tfrac{1}{2}(\dot{U} \pm \dot{U}_1)\mathbf{e}_1 + \tfrac{1}{2}\dot{U}_2\mathbf{e}_2, \tag{A.1c}$$

$$\dot{\mathbf{u}}(-b, x_2) = \dot{\mathbf{u}}(b, x_2) - \dot{U}_1\mathbf{e}_1, \tag{A.1d}$$

$$\dot{\mathbf{u}}(\pm b, 0) = \pm\tfrac{1}{2}\dot{U}_1\mathbf{e}_1, \tag{A.1e}$$

$$\dot{\mathbf{u}}(-x_1, 0) = -\dot{\mathbf{u}}(x_1, 0). \tag{A.1f}$$

While introducing $\dot{U}$, $\dot{U}_1$ and $\dot{U}_2$ as additional degrees of freedom, we can eliminate many of the boundary degrees of freedom as follows. As seen from Fig. 14 and Eq. (A.1a)–Eq. (A.1f), we have three kinds of nodes along the boundary:

- nodes A, C and E with prescribed velocities (A.1a), (A.1c) and (A.1e);
- traction-free, periodic (i.e. internal) nodes along part G with unknown velocities;
- nodes along B, D and F with velocities linked to other nodes (A.1b), (A.1d) and (A.1f).

When we consider quadrilateral finite elements, the vector of nodal velocities of all elements can be expressed as

$$\dot{\mathbf{u}}_e = \begin{pmatrix} \gamma_1\dot{u}_1^{(1)} \\ \gamma_1\dot{u}_2^{(1)} \\ \gamma_2\dot{u}_1^{(2)} \\ \gamma_2\dot{u}_2^{(2)} \\ \gamma_3\dot{u}_1^{(3)} \\ \gamma_3\dot{u}_2^{(3)} \\ \gamma_4\dot{u}_1^{(4)} \\ \gamma_4\dot{u}_2^{(4)} \end{pmatrix} + \dot{U}\begin{pmatrix} \alpha_{11} \\ 0 \\ \alpha_{31} \\ 0 \\ \alpha_{51} \\ 0 \\ \alpha_{71} \\ 0 \end{pmatrix} + \dot{U}_1\begin{pmatrix} \alpha_{12} \\ 0 \\ \alpha_{32} \\ 0 \\ \alpha_{52} \\ 0 \\ \alpha_{72} \\ 0 \end{pmatrix} + \dot{U}_2\begin{pmatrix} 0 \\ \alpha_{23} \\ 0 \\ \alpha_{43} \\ 0 \\ \alpha_{63} \\ 0 \\ \alpha_{83} \end{pmatrix} \equiv \dot{\mathbf{U}}_e + \dot{U}\mathbf{v}_1 + \dot{U}_1\mathbf{v}_2 + \dot{U}_2\mathbf{v}_3 \tag{A.2}$$

with $\dot{u}_i^{(K)}$ denoting the nodal velocity of the independent node K or, if dependent, the node to which the (periodic) node is tied, and $\gamma_i \in [-1, 0, 1]$, $\alpha_{i1} \in [0, 1/2, 1]$, $\alpha_{i2}, \alpha_{i3} \in [-1, 0, 1/2]$. In the same way, the virtual velocities $\delta\dot{\mathbf{u}}_e$ may be written as

$$\delta\dot{\mathbf{u}}_e = \delta\dot{\mathbf{U}}_e + \delta\dot{U}\mathbf{v}_1 + \delta\dot{U}_1\mathbf{v}_2 + \delta\dot{U}_2\mathbf{v}_3. \tag{A.3}$$

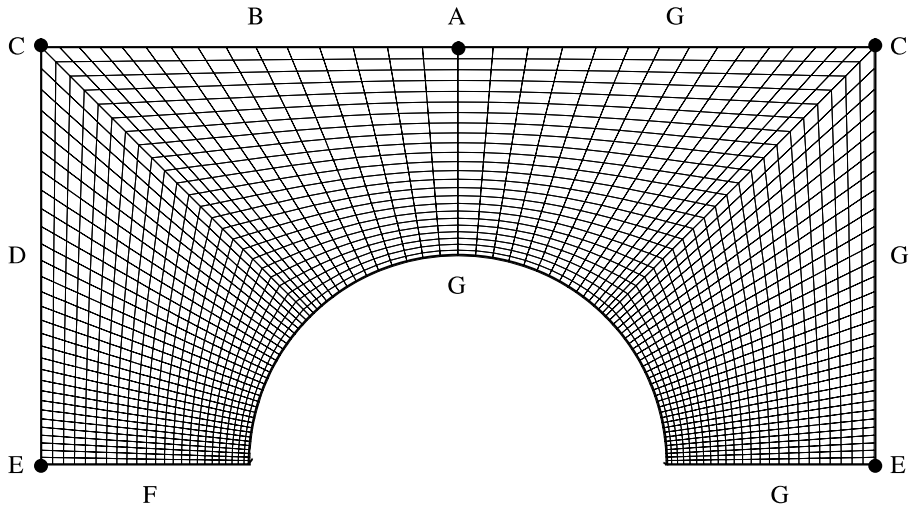

Fig. 14. Detailed view of the mesh in the region to be analysed (Fig. 1) with the various parts of the boundary conditions.

If we denote the stiffness matrix of the element by $\mathbf{R}$ and the element nodal force vector as $\mathbf{f}_e$, the virtual work statement $\delta\dot{\mathbf{u}}_e \cdot \mathbf{R} \cdot \dot{\mathbf{u}}_e = \delta\dot{\mathbf{u}}_e \cdot \mathbf{f}_e$ at the element level becomes

$$\begin{aligned}&(\delta\dot{\mathbf{U}}_e + \delta\dot{U}\mathbf{v}_1 + \delta\dot{U}_1\mathbf{v}_2 + \delta\dot{U}_2\mathbf{v}_3) \cdot \mathbf{R} \cdot (\dot{\mathbf{U}}_e + \dot{U}\mathbf{v}_1 + \dot{U}_1\mathbf{v}_2 + \dot{U}_2\mathbf{v}_3)\\ &\quad = (\delta\dot{\mathbf{U}}_e + \delta\dot{U}\mathbf{v}_1 + \delta\dot{U}_1\mathbf{v}_2 + \delta\dot{U}_2\mathbf{v}_3) \cdot \mathbf{f}_e. \end{aligned} \tag{A.4}$$

Now, Eq. (A.4) is a quadratic expression in $\dot{\mathbf{U}}_e$, $\dot{U}$, $\dot{U}_i$ and $\delta\dot{\mathbf{U}}_e$, $\delta\dot{U}$, $\delta\dot{U}_i$, which may be rewritten as

$$\delta\mathbf{v}' \cdot \mathbf{R}' \cdot \mathbf{v}' = \delta\mathbf{v}' \cdot \mathbf{f}. \tag{A.5}$$

The prime $(\,)'$ denotes the original system of equations extended with three extra degrees of freedom ($\dot{U}$, $\dot{U}_1$ and $\dot{U}_2$): i.e.

$$\mathbf{v}' = \begin{pmatrix} \dot{\mathbf{U}}_e \\ \dot{U} \\ \dot{U}_1 \\ \dot{U}_2 \end{pmatrix}, \quad \delta\mathbf{v}' = \begin{pmatrix} \delta\dot{\mathbf{U}}_e \\ \delta\dot{U} \\ \delta\dot{U}_1 \\ \delta\dot{U}_2 \end{pmatrix}, \quad \mathbf{f}' = \begin{pmatrix} \mathbf{f}_e \\ F \\ F_1 \\ F_2 \end{pmatrix} \tag{A.6}$$

$$\mathbf{R}' = \begin{pmatrix} \mathbf{R} & \mathbf{R}\cdot\mathbf{v}_1 & \mathbf{R}\cdot\mathbf{v}_2 & \mathbf{R}\cdot\mathbf{v}_3 \\ \mathbf{v}_1\cdot\mathbf{R} & \mathbf{v}_1\cdot\mathbf{R}\cdot\mathbf{v}_1 & \mathbf{v}_1\cdot\mathbf{R}\cdot\mathbf{v}_2 & \mathbf{v}_1\cdot\mathbf{R}\cdot\mathbf{v}_3 \\ \mathbf{v}_2\cdot\mathbf{R} & \mathbf{v}_2\cdot\mathbf{R}\cdot\mathbf{v}_1 & \mathbf{v}_2\cdot\mathbf{R}\cdot\mathbf{v}_2 & \mathbf{v}_2\cdot\mathbf{R}\cdot\mathbf{v}_3 \\ \mathbf{v}_3\cdot\mathbf{R} & \mathbf{v}_3\cdot\mathbf{R}\cdot\mathbf{v}_1 & \mathbf{v}_3\cdot\mathbf{R}\cdot\mathbf{v}_2 & \mathbf{v}_3\cdot\mathbf{R}\cdot\mathbf{v}_3 \end{pmatrix}. \tag{A.7}$$

Note that the definition of $\delta\dot{\mathbf{U}}_e$ and $\dot{\mathbf{U}}_e$ according to Eq. (A.2) still contains information about the anti-symmetry in the conditions (A.1a)–(A.1f) through the γ_i. However, since these only define the sign of the nodal velocities, γ_i can be readily incorporated in $\mathbf{R}'$. What we retain is a description wherein all nodes have become internal nodes, while the boundary conditions are applied through the additional three degrees of freedom.

Appendix B

In order to obtain an estimate of the effect of elasticity on macroscopic yield of the 2-D porous material, we follow the analysis of Steenbrink et al. (1997). They considered the macroscopic yield behaviour of a hollow sphere under hydrostatic loading, while we will focus on a hollow cylinder subjected to plane strain equi-biaxial tension.

The initial outer radius of the cylinder is b_0, the radius of the void is a_0. Finite geometry changes are accounted for, and the inner and outer radius are denoted by a and b, respectively. Loading is applied by way of a prescribed constant expansion rate $\dot{b}/b$, and macroscopic yield is assumed to take place at the instant where the corresponding hydrostatic stress Σ_m reaches a maximum. The material of the cylinder is taken to be incompressible and to follow the elastic-viscoplastic behaviour described in Section 2. However, for convenience, the hyperelastic Hooke's law is used rather than the hypoelastic version (since the elastic strains remain relatively small, the difference is negligible for the present purpose). Also, since our main interest here is making an estimation of the instant of macroscopic yield, strain softening and hardening are excluded from the analysis: $h = 0$ and $b_{ij} = 0$. Pressure dependence of yield is neglected also so that $\alpha = 0$.

Because of symmetry, the problem reduces to a (1-D) problem in the radial direction, characterized by the radial coordinate r in the current (deformed) configuration. Due to incompressibility, the deformation can be determined directly through $b^2 - r^2 = b_0^2 - r_0^2$ or $r^2 - a^2 = r_0^2 - a_0^2$, where subscripts '0' denote quantities in the undeformed configuration. The overall dilatation $(b/b_0)^2$ is related to the current void volume fraction $f = (a/b)^2$ (note the difference with $f = (\pi/4)(a/b)^2$ for square unit cell in Section 2) through

$$\left(\frac{b}{b_0}\right)^2 = \frac{1-f_0}{1-f}. \tag{B.1}$$

Also, the rate of deformation can be described in terms of the shear rate $\dot{\gamma} = \sqrt{d_{ij}d_{ij}}$, and expressed in terms of the applied expansion rate $\dot{b}/b$ as

$$\dot{\gamma} = \sqrt{2}\,\frac{\dot{r}}{r} = \sqrt{2}\,\frac{\dot{b}}{b}\rho^{-2}, \quad \rho = \frac{r}{b}. \tag{B.2}$$

Integration of this expression gives the following result:

$$\gamma = -\frac{\sqrt{2}}{2}\ln\left(1 + \left[\left(\frac{b_0}{b}\right)^2 - 1\right]\rho^{-2}\right). \tag{B.3}$$

By virtue of incompressibility of the matrix material, the response is governed solely by the equivalent shear stress τ which can be expressed in this analysis as $\tau = \sqrt{\frac{1}{2}\sigma'_{ij}\sigma'_{ij}} = (-\sigma_r + \sigma_\theta)/2$, with σ_r and σ_θ denoting the radial and tangential components of Cauchy stress, respectively, in the current deformed configuration at r. Equilibrium dictates that

$$\frac{\mathrm{d}\sigma_r}{\mathrm{d}r} + \frac{\sigma_r - \sigma_\theta}{r} = 0 \tag{B.4}$$

with boundary conditions $\sigma_r(a) = 0$ and $\sigma_r(b) = \Sigma_\mathrm{m}$. Expression (B.4) can be integrated, so that the applied hydrostatic stress (normalized by s_0) can be expressed in terms of the current shear stress distribution inside the cylinder as

$$\frac{\Sigma_\mathrm{m}}{s_0} = 2\int_{a/b}^{1}\left(\frac{\tau}{s_0}\right)\frac{\mathrm{d}\rho}{\rho}. \tag{B.5}$$

It is important to realize that the integral is taken over the deformed configuration. In particular, small initial void volume fractions in combination with small macroscopic strains $\ln(b/b_0)$ give rise to a substantial change in the lower bound in Eq. (B.5).

For a purely elastic material, the equivalent shear–stress distribution (normalized by s_0) would be given by

$$\frac{\tau}{s_0} = c\gamma \quad \text{with } c = \frac{\sqrt{2}}{3}\frac{E}{s_0}. \tag{B.6}$$

Substitution of this distribution into Eq. (B.5) with $\gamma = \gamma(\rho)$ from Eq. (B.3) leads to an integral that can be evaluated numerically to give the hydrostatic stress needed for a finite change of void volume. If, on the other hand, the material would only deform viscoplastically, one may immediately use the known distribution $\dot{\gamma}(\rho)$ of the shear rate determined by Eq. (B.2) to construct the distribution of τ inside the sphere by substituting $\dot{\gamma}$ for $\dot{\gamma}^\mathrm{p}$ in Eq. (8); i.e. $\tau = \tau(\dot{\gamma}(\rho))$. In the case of an elastic–viscoplastic material, one will in general find a regime $a/b < \rho < p$ where the response is predominantly viscoplastic, while the outer shell $p < \rho < 1$ is still predominantly elastic. Steenbrink et al. (1997) simplified this distribution by introducing the notion of a plastic front. Then they were able to fit the numerical results with an analytical expression. Borrowing their procedure we were able to fit maxima found from the full numerical solution of Eq. (B.5) by an expression of the form

$$\Sigma_\mathrm{m} = \tau_b e\left[\exp\left(-\frac{1}{e}\ln f_0\right) - 1\right], \tag{B.7}$$

where in the present case, the parameter e is given by

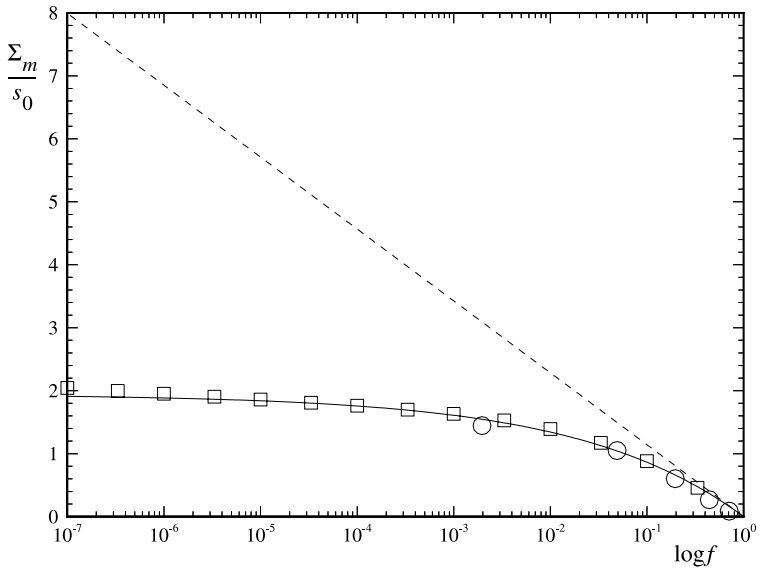

Fig. 15. Maximum hydrostatic stress (Σ/s_0) as function of void volume fraction (f): (□) numerical results according to Eq. (B.5); (○) FE cell calculations with $f = (\pi/4)(a/b)^2$; (—) curve according to Eq. (B.7) and (- - -) original Gurson curve according to Eq. (B.9).

$$e = \frac{5}{4}\left(\ln\left(3\frac{\tau_b/s_0}{E/s_0}\right) + 1\right) \approx \frac{5}{4}\ln(\tau_b/E). \tag{B.8}$$

In the limiting case, that elasticity can be neglected, $\tau_b/E \to 0$, as relevant for instance for ductile metals, we have $e \to -\infty$. Fig. 15 shows the numerical calculations according to Eq. (B.5) together with results from the cell analysis and the curves predicted by Eq. (B.7) and by the original Gurson expression (16). The factor 5/4 in Eq. (B.8) has been introduced in fact to fit the numerical results.

Now, under a purely hydrostatic state of stress, the Gurson yield function (16) yields

$$\frac{\Sigma_{\mathrm{m}}}{\tau_b} = \operatorname{arccosh}\left(\frac{1+f_0^2}{2f_0}\right) = -\ln f_0, \tag{B.9}$$

which originates (Gurson, 1977) from assuming rigid-plastic flow throughout the sphere. From Eq. (B.7) on the other hand, we find

$$-\ln f_0 = e\ln\left(\frac{\Sigma_{\mathrm{m}}}{e\tau_b} + 1\right). \tag{B.10}$$

As we have argued in the main text, due to highly localized deformations, yield is not controlled by the volume fraction but the ligament size. In the cylindrical case, the ligament is characterized by $\Lambda_f = a/b = \sqrt{f}$, and therefore, we rewrite this as

$$-\frac{1}{2}\ln f_0 = -\ln \Lambda_f = \operatorname{arccosh}\left(\frac{1+\Lambda_f^2}{2\Lambda_f}\right) = \frac{e}{2}\ln\left(\frac{\Sigma_{\mathrm{m}}}{e\tau_b} + 1\right), \tag{B.11}$$

i.e. expression (21).

References

Argon, A.S., 1973. A theory for the low-temperature plastic deformation of glassy polymers. Phil. Mag. 28, 839–865.
Bucknall, C.B., 1977. Toughened Plastics. Applied Science, London.
Boyce, M.C., Parks, D.M., Argon, A.S., 1988. Large inelastic deformation of glassy polymers. I. Rate dependent constitutive model. Mech. Mater. 7, 15–33.
Christensen, M.R., 1979. Mechanics of composite materials. Wiley, New York.
Gurson, A.L., 1977. Continuum theory of ductile rupture by void nucleation and growth. I. Yield criteria and flow rules for porous ductile media. J. Engng. Mater. Tech. 99, 2–15.
Haward, R.N., Owen, D.R.J., 1973. The yielding of a two-dimensional void assembly in an organic glass. J. Mat. Sci. 8, 1136–1144.
Jeong, H.-Y., Pan, J., 1995. A macroscopic constitutive law for porous solids with pressure sensitive matrices and its implications to plastic flow localization. Int. J. Solids Struct. 32, 3669–3691.
Koplik, J., Needleman, A., 1988. Void growth and coalescence in porous plastic solids. Int. J. Solids Struct. 24, 835–853.
Lazzeri, A., Bucknall, C.B., 1995. Applications of a dilatational yielding model to rubber-toughened polymers. Polymer 36, 2895–2902.
Needleman, A., 1972. Void growth in an elastic-plastic medium. J. Appl. Mech. 39, 964–970.
Pardoen, T., Hutchinson, J.W., 1999. Improved model for the growth and coalescence of voids in elastoplastic solids. (In preparation).
Leblond, J.B., Perrin, G., 1991. Analytical study of the coalescence of cavities in ductile fracture of metals. In: Anisotropy and localization of plastic deformation, Proceedings of Plasticity. Elsevier, Amsterdam.
Pijnenburg, K.G.W., Steenbrink, A.C., Van der Giessen, E., 1999. Shearing of particles during crack growth in polymer blends. Polymer 40, 5761–5771.
Richelsen, A.B., Tvergaard, V., 1994. Dilatant plasticity or upper bound estimates for porous ductile solids. Acta Metal. Mater. 44, 2561–2577.
Smit, R.J.M., Brekelmans, W.A.M., Meijer, H.E.H., 1999. Prediction of the large-strain mechanical response of heterogeneous polymer systems: local and global deformation behaviour of a representative volume element of voided polycarbonate. J. Mech. Phys. Solids 47, 201–221.
Socrate, S., Boyce, M.C., 2000. Micromechanics of toughened polycarbonate 48, 233–273.
Steenbrink, A.C., Van der Giessen, E., Wu, P.D., 1997. Void growth in glassy polymers. J. Mech. Phys. Solids 45, 405–437.
Steenbrink, A.C., Van der Giessen, E., Wu, P.D., 1998. Studies on the growth of voids in amorphous glassy polymers. J. Mat. Sci. 33, 3163–3175.
Steenbrink, A.C., Van der Giessen, E., 1999. On cavitation, post-cavitation and yield in amorphous polymer-rubber blends. J. Mech. Phys. Solids 47, 843–876.
Sue, H.-J., Yee, A.F., 1988. Deformation behaviour of a polycarbonate plate with a circular hole: finite elements model and experimental observations. Polymer 29, 1619–1624.
Sun, Y., Wang, D., 1989. A lower bound approach to the yield loci of porous materials. Acta Mechanica Sinica 5, 237–243.
Tandon, G.P., Weng, G.J., 1988. A theory of particle reinforced plasticity. J. Appl. Mech 55, 126–135.
Tvergaard, T., 1981. Influence of voids on shear band instabilities under plane strain conditions. Int. J. Fracture 17, 389–407.
Tvergaard, T., 1982. On localization in ductile materials containing spherical voids. Int. J. Fracture 18, 237–252.
Wu, P.D., Van der Giessen, E., 1993. On improved network models for rubber elasticity and their applications to orientation hardening in glassy polymers. J. Mech. Phys. Solids 41, 427–456.
Wu, P.D., Van der Giessen, E., 1996. Computational aspects of localized deformations in amorphous glassy polymers. Eur. J. Mech. A/Solids 15, 799–823.
Zhao, Y.H., Tandon, G.P., Weng, G.J., 1989. Elastic moduli for a class of porous materials. Acta Mechanica 76, 105–131.